A Novel Grid-side AC Fault Ride-Through Control for Multi-Terminal Flexible HVDC Systems

Zainan Li[1], Zhixuan Lin[1], Niancheng Zhou[1], Qianggang Wang[1]*

[1] *Chongqing University State Key Laboratory of Power Transmission Equipment Technology Chongqing, China*

**email address of corresponding author: lizainan@cqu.edu.cn*

Keywords: Fault ride-through; unbalanced active power; Flexible HVDC systems

Abstract

After a grid-side AC fault in a multi-terminal HVDC system, the unbalanced active power accumulated in the grid-side MMC will cause the DC voltage to rise, resulting in a serious risk of power outage. Aiming at this problem, the causes of DC overvoltage are analysed, revealing that the peak DC overvoltage positively correlates with the unbalanced active power. Based on this basis, a novel grid-side AC fault ride-through (FRT) control was proposed in this paper. First, the power safety boundaries for grid-side MMC are established based on the device overcurrent constraints. Then, considering the AC fault voltages and short-circuit ratio, the inner-loop current reference value is given to improve the grid-side MMC transmission power capability. Finally, the performance of the proposed AC FRT control is verified by a hardware-in-the-loop test system. Compared with other methods, the proposed method reduces unbalanced power by up to 23%, which effectively enhances the AC FRT capability and reduces the risk of DC overvoltage.

1 Introduction

In multi-terminal flexible HVDC systems, sub-modules (SMs) within MMCs exhibit weak voltage and current withstand capabilities [1]. When an AC line fault occurs in the grid-side MMC, the output active power of the grid-side MMC decreases rapidly. This leads to significant unbalanced power within the HVDC systems, which is continuously injected into the SMs of each MMC. Consequently, this results in elevated overvoltage magnitude, posing challenges to the safety of the equipment. Techniques for suppressing unbalanced power can be classified into three approaches: applying dynamic braking resistors (DBR), the rapid control of unbalanced power, and temporary energy storage in SM capacitors.

In most practical projects, system power balance is primarily maintained by controlling the heat generation of DBR. Depending on the installation location, there are three typical types of DBR devices. The first type is the chopper DBR, installed in the wind turbine to maintain the DC voltage stability of the wind farm [2]. The second type is the DC-DBR, installed in the DC line, which is divided into centralized and distributed configurations. The distributed type is highly flexible but has high heat dissipation requirements and investment costs [3]. An improved topology was proposed that combines the advantages of centralized and distributed, but increases the control complexity [4]. However, DC DBR only applies to point-to-point HVDC systems and cannot be used in multi-terminal HVDC systems [5]. The third type is the AC-DBR, installed on the AC side of the sending MMC and is a simple structure suitable for onshore HVDC systems [6]. Existing DC projects typically utilize multiple equal-capacity DBRs, which tend to over-input DBRs negatively impacting the HVDC system. Therefore, optimization of DBRs and minimization of input DBRs are necessary to improve the performance of the multi-terminal flexible HVDC systems.

In the HVDC systems, the MMC connected to the wind farm is controlled using voltage-frequency control, while the wind farm power is controlled by the wind farm side voltage source converter (WFVSC). Using the communication channel, the MMC passes the unbalanced power information to the WFVSC to adaptively adjust the output power of the wind farm [7]. However, communication delays and reliability constraints need to be considered [8]. To address these issues, a communication-free voltage reduction control has been proposed [9]. In this approach, the MMC reduces the AC voltage to decrease the active output, but the wind farm output remains unchanged, and the excess power is absorbed by the chopper DBR [10]. When the AC voltage is below the threshold, low-voltage ride-through control is activated, and the wind farm injects reactive power to support the fault voltage. The AC side current increases significantly when the wind farm's reactive power output is large [11]. Additionally, increasing the frequency reduces the output power of the wind farm, but this method may cause DC voltage oscillations and slower power regulation [12].

A novel method for transferring unbalanced power to SM is proposed, leveraging the temporary energy storage capability of SM capacitors and the high controllability of MMCs. However, this approach imposes higher requirements on the SM capacitors, increasing costs [13]. In addition, the interaction between multiple MMCs in a multi-terminal flexible HVDC system is not considered. To overcome the above challenges, a novel grid-side AC FRT is proposed, and the main contributions of this paper are to improve the transmission capability of grid-side MMC, the power boundaries of the grid-side MMC are discussed, and the post-fault inner-loop current rectification value is given.

979-8-3315-8138-1

2. Analysis of dc overvoltage in multi-terminal flexible HVDC systems

2.1 Configuration of multi-terminal flexible HVDC systems

In this paper, the four-terminal HVDC systems project in Zhangbei, China, is used as an example with a ring structure, as shown in Fig. 1.

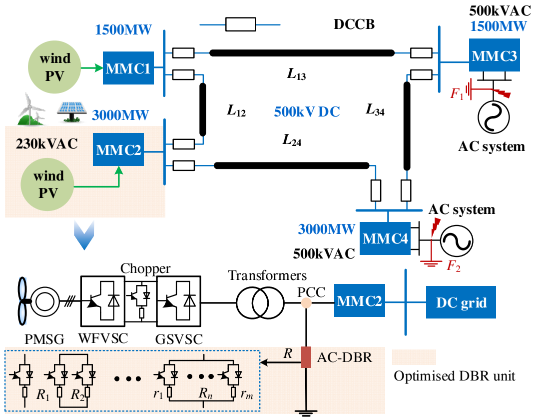

Fig. 1. Topology and control of multi-terminal flexible HVDC systems

MMC1 and MMC2 are connected to renewable energy sources (RESs) as power supply terminals with voltage-frequency control. MMC4 is connected to the AC grid as a power-receiving terminal with constant active power control. MMC3 is used as a power conditioning station by providing a voltage reference to the HVDC systems using constant DC voltage control. AC DBRs are configured on the AC side of MMC2.

Under normal operation, ignoring the internal power loss of the MMC, the active power of the multi-terminal flexible HVDC systems satisfies (1).

$$P_1 + P_2 = P_3 + P_4 + \sum_{i=1}^{4} R_{Li} i_{Li}^2 \tag{1}$$

where MMC1 side P_1 and MMC2 side P_2 are the active powers injected into the HVDC systems by the RESs, MMC3 side P_3 and MMC4 side P_4 are the active powers output from the DC grid, R_{Li} is the line resistance of line Li and i_{Li} is the DC current of line Li.

The AC lines connected to MMC3 and MMC4 are the main transmission channels of the HVDC systems and are mostly overhead lines prone to fault. Definition, F_1 fault: AC line fault on MMC3 side, F_2 fault: AC line fault on MMC4 side.

2.2 Analysis of the DC transient overvoltage problems

Taking the F_2 three-phase fault as an example, the active power at the output of the grid-side MMC4 drops from P_4 to P_{4x}.

$$P_{4x} = (1 - k_{ac4}) P_4 \tag{2}$$

where k_{ac4} is the active power reduction factor, the value of which is related to the degree of AC voltage dips, and takes a value in the range [0,1].

Due to the physical isolation of the HVDC systems, MMC1 and MMC2 provide a stable U_{PCC} and f_{PCC} at the PCC point. Consequently, the output active power of the RESs is unchanged, and the unbalanced active power ΔP of the DC grid can be expressed as (3).

$$\Delta P = P_1 + P_2 - P_{4x} - P_3 - \sum_{i=1}^{4} R_{Li} i_{Li}^2 \tag{3}$$

In the HVDC systems, with the injected power (P_1+P_2) as the reference value, the active power change before and after the F_2 fault is given in Fig. 2. The change in the line power is so small that it is negligible, updating ΔP.

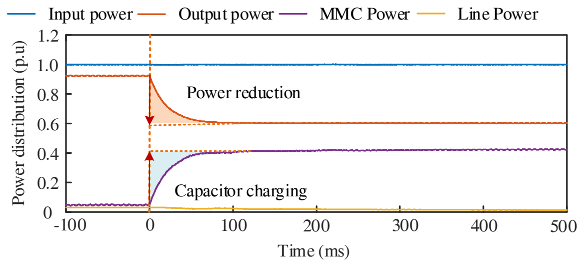

Fig. 2. Active power changes in the HVDC systems after F_2 faults

$$\Delta P = P_1 + P_2 - P_{4x} - P_4 \tag{4}$$

Under the F_2 fault, first, ΔP is injected into the power-regulated MMC3 station, causing the SM capacitor voltage to rise and the DC voltage to rise in the same proportion, and then the remaining MMCs are also injected by ΔP. The DC voltage of the HVDC systems rises further, resulting in the failure of the DC voltage control on the MMC3 side.

It is assumed that the DC voltage increases at the same rate for each MMC, and the energy absorbed by the MMC is affected by the parameters of the SM capacitor.

$$\int_{t=t_0}^{t=t_1} \Delta P dt = \sum_{i=1}^{4} \frac{6C_{eqi}}{2N_i} \left[U_{dc}^2(t_1) - U_{dc}^2(t_0) \right] \tag{5}$$

where T=t_1-t_0 is the fault duration, C_{eqi} is the SM capacitance of MMCi, and N_i is the number of SMs invested in a single bridge arm in MMCi.

The SM capacitor voltage and DC voltage waveforms are shown in Fig. 3, and the DC overvoltage magnitude is positively correlated with the fault duration T and ΔP value.

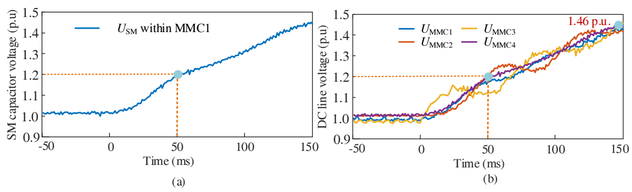

Fig. 3. HVDC systems DC overvoltage waveforms. (a) SM capacitor voltage waveform. (b) DC side Voltage Waveform.

3. Proposed grid-side AC FRT control

3.1 Active and reactive power range for grid-side MMC

Assuming a three-phase grounded F_2 fault on the AC line on the MMC4 side, the equivalent circuit is shown in Fig. 4. The active and reactive powers transmitted by the grid-side MMC are P_{GS} and Q_{GS}, the current injected into the faulted point is I_{GS}, and the current injected into the faulted point by the AC side grid is I_S.

Based on the KVL principle, the relationship equation between the MMC outlet voltage U_{GS} and the fault point voltage U_{fault} is given.

979-8-3315-8138-1

$$\dot{U}_{\text{GS}} = \Delta\dot{U}_{\text{GS}} + \dot{U}_{\text{fault}} = \frac{\hat{S}_{\text{GS}}}{\hat{U}_{\text{GS}}} Z_{\text{T}} + \dot{U}_{\text{fault}} \tag{6}$$

where the superscript ^ is the complex conjugate, and Z_T is the transformer impedance.

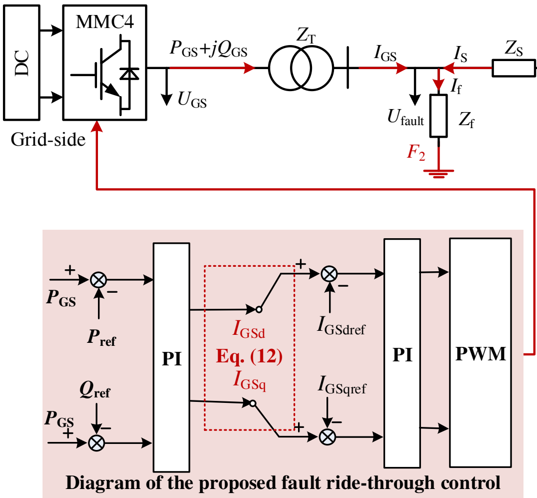

Fig. 4. Schematic diagram of the equivalent circuit for the F_2 fault.

Based on the KCL principle, the fault current relationship is given with the fault point as the node.

$$\dot{I}_{\text{GS}} + \dot{I}_{\text{S}} = \dot{I}_{\text{fault}} \tag{7}$$

$$\frac{\hat{S}_{\text{GS}}}{\hat{U}_{\text{GS}}} + \frac{\dot{U}_{\text{S}} - \dot{U}_{\text{fault}}}{Z_{\text{S}}} = \frac{\dot{U}_{\text{fault}}}{Z_{\text{f}}} \tag{8}$$

where Z_f is the equivalent impedance at the fault point.

The transformer consists mainly of inductance, $Z_T \approx X_T$, the AC line reactance of the AC system is much greater than the resistance, $Z_S \approx X_S$, and the transition resistance at the point of fault is mostly resistive, $Z_f \approx R_f$. Combining (6) and (8) eliminates the variable U_{fault} and gives the relationship between the U_{GS} and the U_S, as shown in (9).

$$\dot{U}_{\text{GS}} = \frac{P_{\text{GS}} - jQ_{\text{GS}}}{\hat{U}_{\text{GS}}} \left(jX_{\text{T}} + \frac{jX_{\text{S}} R_{\text{f}}}{R_{\text{f}} + jX_{\text{S}}} \right) + \dot{U}_{\text{S}} \frac{R_{\text{f}}}{R_{\text{f}} + jX_{\text{S}}} \tag{9}$$

The value of U_{GS} value is affected by R_f, X_S, U_S, P_{GS} and Q_{GS}. After the F_2 fault, the AC system is equivalent to a constant voltage source and the MMC is equivalent to a current source. To constrain the I_{GS} amplitude peaks, the grid-side MMC removes the outer control loop and is given the inner loop current d axis and q axis reference values. Due to the fast control response of the inner current loop, it can be assumed that the actual AC current can follow the reference values in real time.

Considering the safety of the insulated gate bipolar transistor, a limiter is added to the MMC current inner loop, and the active current I_{GSd} and reactive current I_{GSq} satisfy the following conditions.

$$I_{\text{GS}d}^2 + I_{\text{GS}q}^2 \le I_{\max}{}^2 \tag{10}$$

where I_{max} is the peak AC current injected into the fault point by the MMC, determined by the overcurrent coefficient k_{max} together with the AC rated current I_{ACN}.

$$I_{\max} = k_{\max} I_{\text{ACN}} \tag{11}$$

In the dq-axis coordinate system, the q-axis AC voltage component U_{GSq} is 0. Based on the instantaneous power theory, the equations for P_{GS} and Q_{GS} are given, and the constraints for the grid-side MMC are given by multiplying U_{GS} on (10).

$$P_{\text{GS}} = \frac{3}{2} U_{\text{GS}} I_{\text{GS}d} \quad Q_{\text{GS}} = -\frac{3}{2} U_{\text{GS}} I_{\text{GS}q} \tag{12}$$

$$P_{\text{GS}}^2 + Q_{\text{GS}}^2 \le \frac{3}{2} I_{\max}^2 U_{\text{GS}}^2 \tag{13}$$

Using (9) and (13), the boundary ranges of P_{GS} and Q_{GS} for the grid-side MMC output are given, and the P_{GS} and Q_{GS} values are affected by the R_f, X_S and U_S values.

$$P_{\text{GS}}^2 + Q_{\text{GS}}^2 + aP_{\text{GS}} + b\text{Q}_{\text{GS}} + c \le 0 \tag{14}$$

where the relevant parameters a, b and c are shown in (A1).

The short-circuit ratio of a grid-side MMC connected AC system is defined as.

$$\lambda = \frac{S_{\text{AC}}}{P_{\text{GS0}}} = \frac{U_S^2}{X_S P_{\text{GS0}}} \tag{15}$$

where S_{AC} is the short-circuit capacity on the AC side and P_{GS0} is the active power transmitted by the MMC before the F_2 fault.

The fault current I_f consists of both I_S and I_{GS}, and the diagram of each current phase for different operating conditions of the grid-side MMC is given in Fig. 5. θ is determined by the active and the reactive power.

$$\theta = \arctan \frac{Q_{\text{GS}}}{P_{\text{GS}}} \tag{16}$$

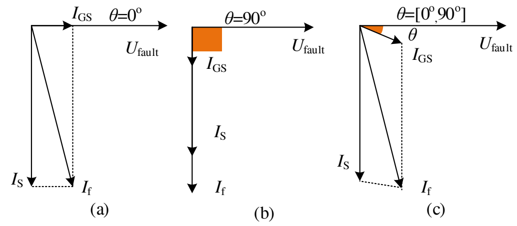

Fig. 5 Fault currents under different operating conditions of grid-side MMC. (a) MMC only generates active power. (b) MMC only generates reactive power. (c) MMC generates active and reactive power.

The power sending MMC is mostly connected to the strong grid and it is considered that λ>>3. The strong grid has strong support for U_{fault}, the contribution proportion of I_S in I_f is high, and the neglect of I_{GS} has less influence on the magnitude of I_f. Neglecting the voltage drop of X_T, U_{GS} is equal to U_{fault}, determined by the transition resistor R_f and U_S.

$$U_{\text{GS}} \approx U_{\text{fault}} \approx \frac{R_f U_{\text{S}}}{\sqrt{R_{\text{f}}^2 + X_{\text{S}}^2}} \tag{17}$$

Bringing (17) into (14) gives the P_{GSmax} values, and the post-fault P_{ref} value is taken as the minimum of P_{GS0} before the fault and P_{GSmax}, Q_{ref} is calculated by bringing P_{ref} into (14), as shown in Fig. 6. Then, I_{GSd} and I_{GSq} are given using (12).

$$P_{\text{ref}} = \min\left(P_{\text{GS0}} \quad P_{\text{GSmax}}\right) \tag{18}$$

Due to MMC4 is a power receiving terminal, it only outputs P_{ref} and Q_{ref} in the first quadrant. As U_{GS} decreases, the controllable range of P_{ref} and Q_{ref} decreases as shown in Fig. 6(a). As the value of k_{max} increases, the values of P_{ref} and Q_{ref} increase significantly as shown in Fig. 6(b). The variation of P_{ref} and Q_{ref} with λ is shown in Fig. 6(c).

979-8-3315-8138-1

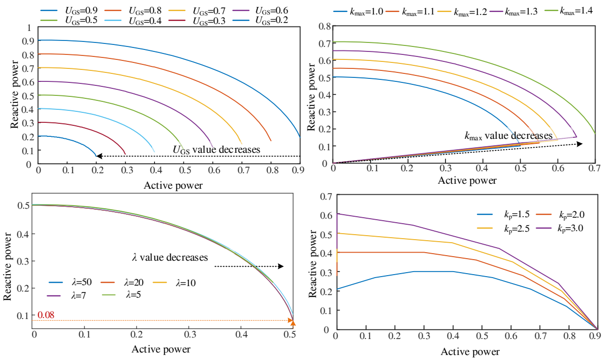

Fig. 6. P_{ref} and Q_{ref} regions for MMC outputs. (a) Changes in P_{ref} and Q_{ref} under different U_{GS}s. (b) Changes in P_{ref} and Q_{ref} under different k_{max}. (c) Changes in P_{ref} and Q_{ref} under different λ. (d) Changes in P_{ref} and Q_{ref} under different k_p in [11].

In the conventional method, a reference value for the current in the q axis of the inner loop of the current is given [14], with priority given to providing Q_{ref}, and the ranges of P_{ref} and Q_{ref} are shown in Fig. 6(d).

$$I_{GSq} = k_q(0.9 - U_{GS})I_{ACN} \quad (19)$$

where k_p is the reactive power coefficient whose value is taken as 1.5~3.0.

3.2 Estimation of unbalanced active power ΔP

In steady state operation of the HVDC system, the L_{13} and L_{24} lines transmit most of the active power, and the power interacted by MMC1 and MMC2 is small. Therefore, under F_1 and F_2 faults, the voltage difference between U_1 and U_2 is small and satisfies $U_1 \approx U_2$.

The DC voltage fluctuation under steady state operation of the system is less than 0.05 p.u., set U_{SET}=1.05 p.u. Only ΔP is injected into the SM before the DC voltage reaches U_{SET}. Select the DC voltage data in the interval T_0~T_{SET} and determine ΔU_2 to calculate the energy absorbed by MMC2, as shown in Fig. 7.

$$\Delta W_{MMC2} = 0.5C_{eq}U_{SET}^2 - 0.5C_{eq}U_2^2 \quad (20)$$

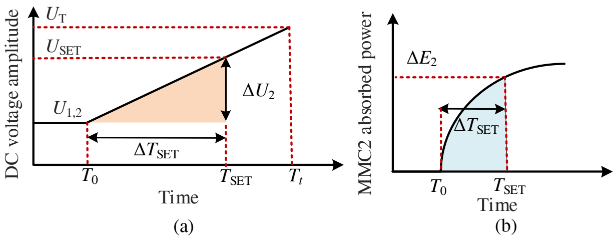

Fig. 7. The relationship between ΔP and u_{SMT}; Fig. (a) shows theΔP; Fig. (b) shows the u_{SMT} growth trend

MMC1 and MMC2 sides use the local information to derive the ΔP.

$$\Delta P = \frac{\Delta W_{MMC2}}{\Delta T_{SET}}\left(1 + \frac{N_2\left(\frac{C_{eq1}}{N_1} + \frac{C_{eq3}}{N_3} + \frac{C_{eq4}}{N_4}\right)}{C_{eq2}}\right) \quad (21)$$

P_1 and P_2 are controlled by the wind farm, which is difficult to control, while P_4 can be easily realized by adjusting the power outer loop.

Under the F_2 fault, the power regulating station MMC3 follows the power variation up to the upper limit value. While in F_1 fault, the fixed power station MMC4 maintains the pre-fault active power, it is necessary to determine whether MMC4 has the power margin to reduce ΔP.

4. Simulation test and results analysis

The efficacy of the proposed AC FRT is evaluated in four-terminal flexible HVDC systems simulated within the RTDs as shown in Fig. 8, and the detailed system parameters are shown in TABLE 1. Assume λ=7, k_p=2.0, k_{max}=1.2, and fault duration is 200ms. Three methods are set up: method 1 (M1): the proposed AC FRT control; method 2 (M2): ΔP is absorbed by four groups of equal capacity AC DBR on MMC2 side [6]; method 3 (M3): MMC1 and MMC2 reduce the AC voltage and ΔP is absorbed by the chopper DBR [15]. When the DC voltage exceeds 1.1 p.u., M2 and M3 are immediately activated, giving the reactive active power of the grid-side MMC in accordance with [11].

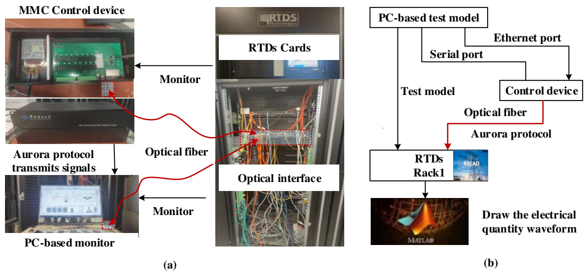

Fig. 8. RTDs test validation. (a) Physical structure of the experimental test system. (b) Test logic diagram.

TABLE I
HBSM-MMC-HVDC SYSTEM PARAMETERS

Parameter	Parameters size
Rated dc voltage	±500 kV
MMC1 and MMC2 control mode	VF control
MMC3 control mode	DC voltage control
MMC4 control mode	Active power control
MMC1 rating capacity	1500 MVA
MMC3 rating capacity	1100 MVA
MMC2 and MMC4 rating capacity	3000 MVA
AC voltage modulation ratio of MMC1 to MMC4 /m_{ac}	0.85
Bridge arm inductors/L_{arm}	50 mH
Equal capacitance discharge time constant/T_C	30 ms
SM on-state resistance	0.001Ω
CLR/L_{dc}	150 mH
Line length	300 km
Line Sampling frequency	10 kHz
The number of SMs in the MMC	200

Under F_2 fault, assuming U_{fault}=0.19 p.u., in M1, I_{GSd}=1.09 p.u., I_{GSq}=0.47 p.u. are given, while in M2 and M3, I_{GSd}=0.0 p.u., I_{GSq}=1.2 p.u. are given.

Fig. 9(a) gives the active power transmitted by the grid-side MMC4 under different methods, where MMC4 reduces the transmitted power to 0 MW under M2 and M3, while the active power is reduced by 1160 MW under M1, and it still maintains the 340 MW transmission, which improves the transmission capability by 23.0%. It shows that the proposed method can effectively improve the transmission capacity of the grid-side MMC. Using (21), MMC2 estimates ΔP to be 1161 MW.

The active power for different methods is shown in Fig. 9(b) and (c). In M2, the P_3 is adaptively increased to 500

979-8-3315-8138-1

MW, the MMC2 side AC DBR is fully inputted and absorbs 1400 MW from the wind farm to match ΔP, and the energy absorbed by the DBR is 23.8 MJ. In M3, MMC1 and MMC2 detect the DC voltage amplitude to reduce the AC voltage to match the ΔP. At this time, the AC voltage is lower, the wind farm enters into the deep low voltage ride-through state, more reactive power is injected into the wind farm, and the active power absorbed by the chopper DBR is more than 2000 MW, and the energy absorbed by the DBR is 40.8 MJ, as shown in Fig. 9(d). In the proposed method M1, the AC voltages of MMC1 and MMC2 are slightly reduced, and the wind farm does not need to inject reactive power, and the active power absorbed by the chopper DBR ΔP_1 is determined to be 210 MW. Using the improved non-equal AC DBR to absorb the ΔP_2, ΔP_2=900 MW, and the energy absorbed by the DBR is 20.0 MJ. Compared to M2 and M3, the energy absorbed by the proposed method is reduced by 16.0% and 51.0%, respectively. Fig. 9(e) gives the DC voltage waveforms for the three methods, all fluctuating above and below 1.1 p.u. and not exceeding 1.15 p.u.

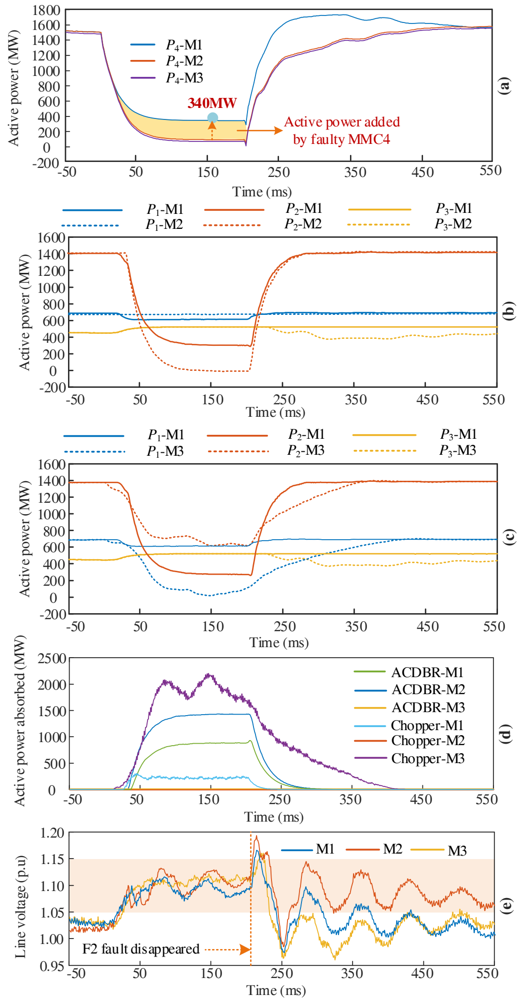

Fig. 9. Analysis of test results for F_2 faults. (a) is the active power transmitted by the grid-side MMC. (b) is the active power of the DC grid under M1 and M2. (c) is the active power of the DC grid under M1 and M3. (d) is the energy absorbed by DBR. (e) is the DC voltage waveform.

Fig. 10 gives the AC current waveforms of different methods, when k_{max} is determined, the current amplitude is similar under different methods.

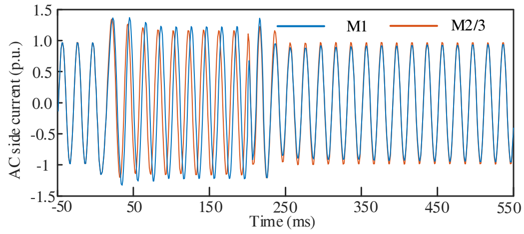

Fig. 10. Grid-side MMC AC current waveform under different methods

4 Conclusion

In this paper, a novel grid-side AC FRT control for multi-terminal DC grids is proposed. Firstly, the active and reactive power safety boundaries of the grid-side MMC are established, taking into account U_{falut} and λ, and the reference values of active and reactive currents of the current inner loop are given. Test results show that in the proposed method, the active of the grid-side MMC is reduced by up to 23% of ΔP.

In the future, consideration must be given to extreme fault conditions where the fault voltage drops to zero, analysing the impact on device overvoltage and overcurrent. Furthermore, the effect of AC-DC coupling on unbalanced power must also be taken into account.

This work is supported by National Key Technology Special Project for Smart Grid (2024ZD0802800), China Postdoctoral Science Foundation (2025M780490)

6 References

[1] Z Li, K Jia, T Bi, et al. " Adaptive Current Limiting Control in Half-Bridge MMC for DC Fault." in IEEE Transactions on Industrial Electronics, vol. 72, no. 1, pp. 516-524, 2025.

[2] A Egea-Àlvarez, M Aragüés-Peñalba, E Prieto-Araujo, et al. "Power reduction coordinated scheme for wind power plants connected with VSC-HVDC. " in Renewable energy, vol. 107, p. 1-13, 2017.

[3] J Ouyang, J Chen, J Yu, et al. "Security Region Modeling and Fault Ride-Through Coordinative Control of VSC-HVDC under Grid Fault." in IEEE Transactions on Power Delivery, vol. 38, no. 5, pp. 3701-3711, 2023.

[4] S Wu, L Qi, M Jin, et al. "An MMC With Integrated Energy Dissipation Function Using Thyristor-Based Chopper Modules for the Offshore Wind VSC-HVDC System." in IEEE Transactions on Power Electronics, vol. 39, no. 1, pp. 1609-1623, 2024.

[5] X Wang, R Yang, Z Shi, et al. "Coordinated low voltage ride-through of MMC-HVDC transmission system and wind farm with distributed braking resistors." in IEEE Access, vol. 10, pp. 87860-87869, 2022.

[6] S Cao, X Zhang, W Xiang, et al. "A power flow transfer entropy based AC fault detection method for the MTDC wind power integration system." in IEEE Transactions on Industrial Electronics, vol. 68, no. 11, pp. 11614-11620, 2021.

[7] S Nanou, S Papathanassiou. " Evaluation of a communication - based fault ride - through scheme for offshore wind farms connected through high-voltage DC links based on voltage source converter." in IET Renewable Power Generation, vol. 9, no. 8, pp. 882-891, 2015.

979-8-3315-8138-1

[8] U Karaagac, J Mahseredjian, L Cai, et al. "Offshore wind farm modeling accuracy and efficiency in MMC-based multiterminal HVDC connection." in IEEE Transactions on Power Delivery, vol. 32, no. 2, pp. 617-627, 2017.

[9] A Moawwad, M S El Moursi, W Xiao. "Advanced fault ride-through management scheme for VSC-HVDC connecting offshore wind farms." in IEEE Transactions on Power Systems, vol. 31, no. 6, pp. 4923-4934, 2016.

[10] M B Silva, C L Moreira, H Leite, et al. "Control strategies for AC fault ride through in multiterminal HVDC grids ." in IEEE Transactions on Power Delivery, vol. 29, no. 1, pp. 395-405, 2014.

[11] K Jia, X Dong, Z Wen, et al. "Harmonic Injection Based Fault Ride-through Control of MMC-HVDC Connected Offshore Wind Farms," in IEEE Transactions on Sustainable Energy, vol. 14, no. 3, pp. 1796-1806, 2023.

[12] M Zhu, W Li, X Liang, et al. " Stepwise voltage drop and transient current control strategies to enhance fault ride-through capability of MMC-HVDC connected DFIG wind farms. " in IEEE Transactions on Power Systems, vol. 36, no. 3, pp. 2127-2137, 2021.

[13] H Zhou, W Yao, M Zhou, et al. "Active Energy Control for Enhancing AC Fault Ride-Through Capability of MMC-HVDC Connected With Offshore Wind Farms." in IEEE Transactions on Power Systems, vol. 38, no. 3, pp. 2705-2718, 2023.

[14] Standardization administration, "Technical specification for connecting wind farm to power system-Part 1:On shore wind power." In China,GB/T 19963.1, 2021.

[15] M B Silva, C L Moreira, H Leite, et al. "Control strategies for AC fault ride through in multiterminal HVDC grids ." in IEEE Transactions on Power Delivery, vol. 29, no. 1, pp. 395-405, 2014.

979-8-3315-8138-1